

Improved Photoelectric Performance of UV Photodetector Based on ZnO Nanoparticle-Decorated BiOCl Nanosheet Arrays onto PDMS Substrate: The Heterojunction and $\text{Ti}_3\text{C}_2\text{T}_x$ MXene Conduction Layer

Weixin Ouyang, Jiaxin Chen, Jr-Hau He, and Xiaosheng Fang*

Large-area BiOCl nanosheet arrays grown on Cu substrate are transferred onto the polydimethylsiloxane (PDMS) substrate, while the as-fabricated BiOCl/PDMS photodetector (PD) yields negligible photocurrents under UV light illumination. The introduction of a $\text{Ti}_3\text{C}_2\text{T}_x$ MXene conduction layer at the interface increases both the photocurrent and dark current by 2–3 orders of magnitude. But this PD suffers from a large dark current (6.7 pA), a low on–off ratio (2.4), and a long decay time (6.87 s) under 350 nm light illumination at 5 V. After the deposition of ZnO nanoparticles (NPs), the optimized PD achieves a low dark current of 86 fA, a high on–off ratio of 7996.5, and a short decay time of 0.93 s. Additionally, the elimination of the $\text{Ti}_3\text{C}_2\text{T}_x$ MXene layer causes decreased photocurrent and prolonged decay time. The greatly improved photoresponse and response speed of these PDs are ascribed to the increased light absorption brought by the ZnO NPs, the improved carrier separation promoted by the ZnO–BiOCl heterojunction, and the efficient carrier pathways provided by the $\text{Ti}_3\text{C}_2\text{T}_x$ MXene conduction layers. The construction of heterojunctions and introduction of conduction additives improve the photodetecting performance of these BiOCl-based PDs, promoting their practical applications in the photoelectric devices.

devices,^[5–7] owing to their layered structures and excellent optical, catalytic, and electrical properties.^[8,9] The layered structure and the as-induced dipole can cause the efficient separation of the electron–hole pair, which can achieve enhanced photocatalytic activity and photoconductivity.^[10,11] The low-dimensional nanostructures of bismuth oxide halides, such as nanosheets,^[12] nanonetworks,^[13] microspheres,^[14] and nanosheet arrays,^[15] have been prepared and adopted as the sensitive materials for photoelectric devices. Depending on diverse preparation methods, the bandgap of BiOCl nanomaterials varies from 3.0 to 3.5 eV, making the BiOCl nanostructures promising candidates for UV-A light detection.^[16,17] Li and his colleagues prepared microsized BiOCl square nanosheets and assembled individual BiOCl nanosheet as an UV photodetector (PD).^[18] However, the photocurrent of this PD increases to 3.3 pA at 30.0 V upon UV illumination, depicting a

quite poor photoresponse. Besides, the low photocurrent value in this order of magnitude is difficult to be measured, thus hindering its practical application.

2D nanosheet arrays have attracted numerous attentions in photoelectric devices for their superior photoelectric properties derived from their high orientation, high surface-to-volume ratios, and open-edge geometry.^[19,20] To acquire elevated photoelectric performance of BiOCl-based PDs, BiOCl nanosheet arrays grown on Cu foil were prepared and fabricated as PDs with different electrode configurations.^[21] However, the direct growth of BiOCl nanosheet on a reactive substrate has distinct drawbacks. It is reported that the monoclinic phase Bi byproduct and residual cubic phase BiCl_3 were examined in the BiOCl/Cu sample after the growth process. Moreover, the exposed Cu foil beneath the BiOCl nanosheet arrays becomes reactive in ambient after the dissolution of its surface, the emergence of Cu-related reaction products such as Cu_2O , CuO , and $\text{Cu}_2(\text{OH})_2\text{CO}_3$ might cause the failure of photoelectric devices. Besides, the interface between the BiOCl nanosheet array and the solid Cu substrate has great influences on the carrier transport process. In the growth process, the dissolution of Cu foil

1. Introduction

Bismuth oxide halides, BiOX ($X = \text{Cl}, \text{Br}, \text{and I}$), consist of tetragonal $[\text{Bi}_2\text{O}_2]^{2+}$ positive slabs interleaved by double negative slabs of halide atoms along the c axis.^[1] They have been widely applied as photocatalysts,^[2] electrocatalysts,^[3] as well as electrode materials in energy storage^[4] and photoelectrochemical

Dr. W. X. Ouyang, J. X. Chen, Prof. X. S. Fang
Department of Materials Science
Fudan University
Shanghai 200433, P. R. China
E-mail: xshfang@fudan.edu.cn

Prof. J. H. He
Department of Materials Science and Engineering
City University of Hong Kong
Kowloon, Hong Kong SAR 999077, P. R. China

 The ORCID identification number(s) for the author(s) of this article can be found under <https://doi.org/10.1002/aelm.202000168>.

DOI: 10.1002/aelm.202000168

into Cu^{2+} ion at the substrate surface and the formation of BiOCl nanocrystals at the reaction sites take place at the same time, thus the newly formed BiOCl nanosheet and the remaining Cu foil located near the interface would suffer from poor crystallinity and inevitable defects, which hinders the carrier transport and increases the recombination possibility of photoinduced charge carriers. To eliminate these negative effects, it is reasonable to get rid of this reactive Cu substrate. Considered the poor structure stability of the self-standing BiOCl nanosheet arrays, the BiOCl nanosheet array without Cu substrate could be transferred onto easy-curing and nonreactive polymer substrates such as polydimethylsiloxane (PDMS), thus their hybrid would not suffer from the undesirable by-products and side effects, while the structural integrity of the BiOCl nanosheet arrays could be retained.^[22,23]

However, the PD fabricated from the self-standing BiOCl nanosheet arrays is reported to present very poor photoelectric performance, because the carrier transport is hindered by the grain boundaries between neighboring nanosheets. To pursue more efficient carrier transport and less carrier recombination, a conduction layer is introduced at the interface between BiOCl nanosheet array and PDMS substrate, so the photoinduced charge carriers can go through individual BiOCl nanosheets from one end to the other end, instead of the grain boundaries before their arrivals at the electrodes. MXenes comprised of transition metal carbides, carbonitrides, and nitrides, are a new family of 2D materials.^[24,25] MXenes possess hydrophilic surfaces and they can achieve high metallic conductivities of $\approx 6000\text{--}10\,000\text{ S cm}^{-1}$, showing great potentials in catalysis,^[26] memristor,^[27] sensors,^[28–30] energy harvester,^[31,32] energy storage devices,^[33,34] conducting thin films,^[35] and so on. The most commonly reported $\text{Ti}_3\text{C}_2\text{T}_x$ ($T = \text{OH}, \text{O}, \text{and F}$) MXene is usually produced by the wet-chemical etching of Al from Ti_3AlC_2 using HF acid, it has been widely applied as sensitive materials and electrodes in PDs.^[36–39] Therefore, the $\text{Ti}_3\text{C}_2\text{T}_x$ MXene flakes can also be adopted to form a conduction layers between the PDMS substrate and the BiOCl nanosheet arrays, aiming to promote the efficient transport of photoinduced charge carriers in the hybrid PDs.

In addition, to promote the applications of BiOCl nanomaterials in photoelectric devices, further investigations and modifications to elevate their performance are badly required. Heterojunctions formed between different semiconductor materials have broad applications in solar cells, photoelectrochemical cells, PDs, and other photovoltaic devices, due to their profound influences on electronic properties and potentials in multifunctions and property tuning.^[40–42] The built-in electric fields created near the interfaces in heterojunctions, can efficiently separate photogenerated electron–hole pairs and regulate the carrier transportation in photoelectric devices based on p–n junctions.^[43,44] ZnO is one of the well-known n-type semiconductor materials with broad applications in the photovoltaic, optoelectronic, and piezoelectric devices.^[45] Owing to its wide bandgap, high exciton binding energy (60 meV), and high photoconductive characteristic, ZnO nanostructures are frequently adopted to construct UV PDs.^[46,47] Moreover, the heterostructure PDs involving ZnO nanostructures have been widely reported and present impressive photoelectric performance,^[48–51] thus combining BiOCl nanosheet arrays with ZnO

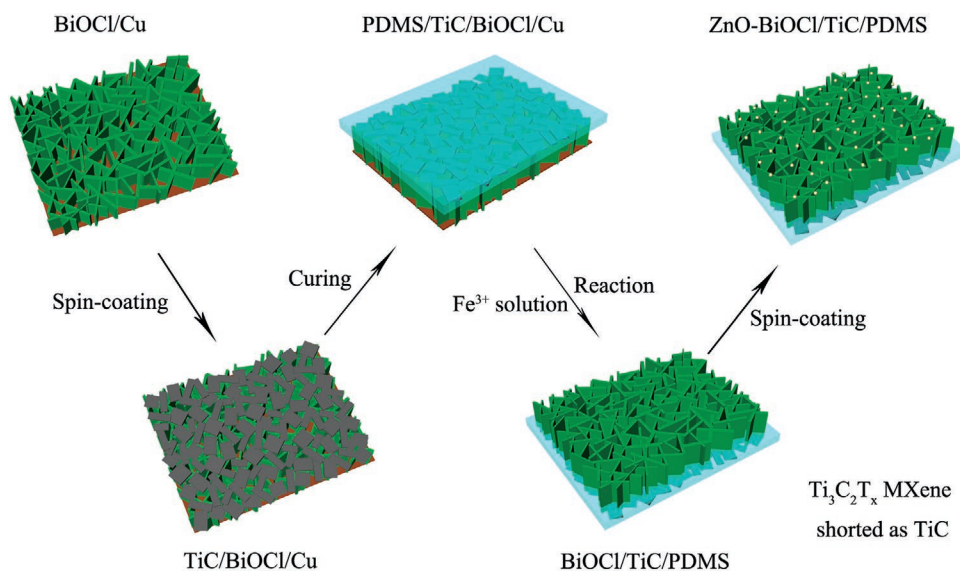
nanostructures to construct p–n junction is reasonable and feasible. Among various nanostructures, ZnO nanoparticles (NPs) are easy to be prepared and deposited evenly on the BiOCl nanosheet array, which are considered as suitable building blocks for heterostructures.

Herein, BiOCl nanosheet arrays onto the PDMS substrate are prepared on a large scale by the etching of Cu foil and curing of the PDMS substrate, while the as-fabricated BiOCl/PDMS PD shows very poor photoelectric performance under UV light illumination. The addition of a $\text{Ti}_3\text{C}_2\text{T}_x$ MXene (shorted as TiC) conduction layer increases both the photocurrent and dark current by 2–3 orders of magnitude. But this BiOCl/TiC/PDMS PD suffers from a large dark current (6.7 pA), a low on–off ratio (2.40), and slow decay time (6.87 s) under 350 nm light illumination at 5 V. After the deposition of ZnO NPs, the optimized ZnO–BiOCl/TiC/PDMS PD (S9) achieves a low dark current of 0.086 pA, a high on–off ratio of 7996.5, and a short decay time of 0.93 s. Besides, the elimination of $\text{Ti}_3\text{C}_2\text{T}_x$ MXene layer causes the decreased photocurrent and prolonged decay time of these PDs. It is believed that the greatly improved photoreponse and response speed of the ZnO–BiOCl/TiC/PDMS PDs are ascribed to the increased light absorption brought by the deposition of ZnO NPs, the promoted carrier separation caused by the heterojunction formed between ZnO NPs and BiOCl nanosheet array, and the efficient carrier pathways provided by the $\text{Ti}_3\text{C}_2\text{T}_x$ MXene conduction layers. The construction of heterojunctions and the introduction of conduction layers are demonstrated to improve the photodetecting performance of these BiOCl-based PDs, paving ways for their practical applications in the photoelectric devices.

2. Results and Discussion

As displayed in **Scheme 1**, a certain amount of $\text{Ti}_3\text{C}_2\text{T}_x$ MXene (shorted as TiC) colloid solution as conducting additives is spin-coated on the BiOCl/Cu sample to prepare the TiC/BiOCl/Cu sample. After the PDMS precursor is cured on the sample and the underlying Cu foil is removed by reaction with Fe^{3+} , the BiOCl/TiC film onto the PDMS substrate is obtained. Then, ZnO NPs are spin-coated on the above samples for different cycles to fabricate a series of ZnO–BiOCl/TiC/PDMS samples. It is worth noting that large-area BiOCl/Cu sample can be fabricated in a feasible way, so is the ZnO–BiOCl/TiC/PDMS sample. Because the PDMS substrate is easy to operate and transfer, the final samples can be cut into pieces with different shapes and areas as desired. These samples are then assembled into corresponding PDs.

Figure 1a demonstrates the X-ray diffraction (XRD) patterns of the BiOCl/Cu and the BiOCl/PDMS samples. For both samples, the characteristic diffraction peaks of BiOCl phase emerge at 2θ of 25.9° , 32.5° , and 33.4° , which correspond to the (101), (110), and (102) crystal facets of tetragonal phase BiOCl (JCPDF 06-0249), respectively. The sharp and narrow diffraction peaks from the BiOCl phase indicate its high crystallinity. After the transfer of BiOCl nanosheet arrays from the Cu foil onto the PDMS substrate, the diffraction peaks of monoclinic phase Bi (JCPDF 65-1215) at 2θ of 28.5° and 55.8° , cubic phase BiCl_3 (JCPDF 11-0600) at 2θ of 47.5° , and cubic phase Cu



Scheme 1. Preparation processes of the BiOCl/TiC/PDMS samples and the ZnO–BiOCl/TiC/PDMS samples.

(JCPDF 04-0836) at 2θ of 50.4° have not been detected. The negative effects of these byproducts and residues on the photoelectric performance of BiOCl-based photodetectors hence can be excluded. The XRD patterns of the Ti_3AlC_2 powder and the as-prepared $\text{Ti}_3\text{C}_2\text{T}_x$ MXene sample are depicted in Figure S1 (Supporting Information). After the etching process, most of the characteristic diffraction peaks of the Ti_3AlC_2 powder are nearly absent. Especially, in agreement with the previous reports,^[24,36] the (002) peak of the Ti_3AlC_2 powder is down shifted from 2θ of 9.6° to 2θ of 6.0° of the $\text{Ti}_3\text{C}_2\text{T}_x$ MXene sample, which proves the removal of Al and introduction of surface terminations. Thus, the successive transformation from the Ti_3AlC_2 precursor to the completely exfoliated $\text{Ti}_3\text{C}_2\text{T}_x$ MXene sample is confirmed. Figure 1b presents the XRD patterns of the ZnO NP sample, the BiOCl/PDMS sample, and a series of ZnO–BiOCl/TiC/PDMS samples. The diffraction peaks of the prepared ZnO sample match well with the hexagonal phase ZnO (JCPDF 65-3411), the diffraction peaks at 2θ of 31.8° , 34.4° , and 36.3° are indexed to the (100), (002), and (101) crystal facets, respectively. The broad diffraction peaks from the ZnO sample indicate that the ZnO phase is composed of small

building blocks. For the ZnO–BiOCl/TiC/PDMS samples, the intensities of diffraction peaks of the ZnO phase at 2θ of 31.8° and 36.3° increase gradually with the increased deposition cycles of ZnO NPs.

Figure 2 shows the morphology of the BiOCl/Cu sample and some of the ZnO–BiOCl/TiC/PDMS samples (S3, S9, and S15). It is observed from the top-view scanning electron microscopy (SEM) image of the BiOCl/Cu sample in Figure 2a that the BiOCl film is composed of vertically aligned and densely cross-linked nanosheets. The magnified image in the inset shows smooth and even BiOCl nanosheets with lateral lengths of several micrometers and thicknesses of less than 100 nm. Figure S2a (Supporting Information) depicts the SEM images of the BiOCl/Cu sample deposited with the $\text{Ti}_3\text{C}_2\text{T}_x$ MXene nanoflakes. It can be seen that the BiOCl nanosheet arrays are evenly covered by a dense and flat layer formed by the $\text{Ti}_3\text{C}_2\text{T}_x$ MXene nanoflakes, which can assure the intimate electrical contact of two phases. After the curing of the PDMS layer and dissolving of Cu substrate, different amounts of ZnO NPs were deposited on the BiOCl/TiC/PDMS samples by spin-coating for various cycles. For the S3 sample with three deposition

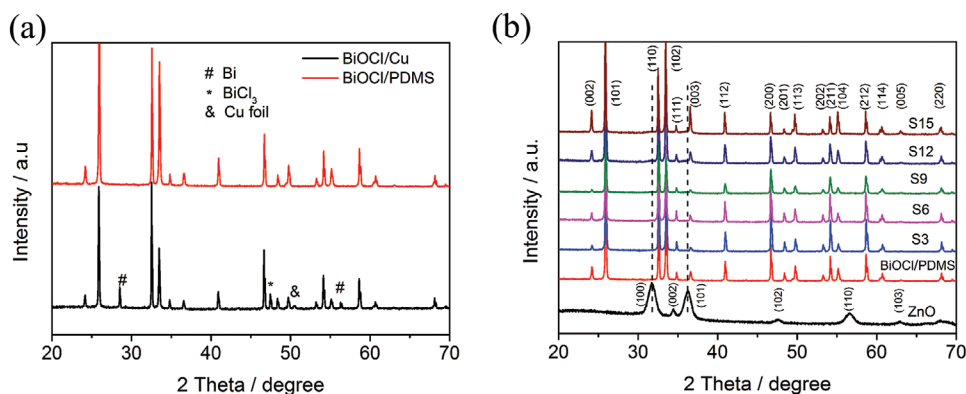


Figure 1. a) XRD patterns of the BiOCl samples with different substrates. b) XRD patterns of the ZnO sample and the ZnO–BiOCl/TiC/PDMS samples.

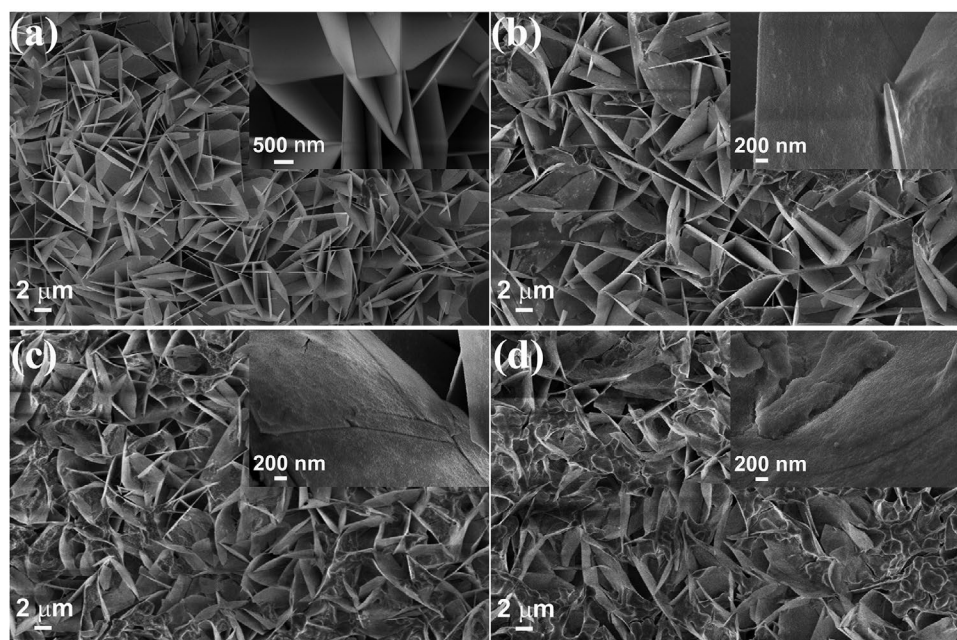


Figure 2. SEM images of a) the BiOCl/TiC/PDMS sample and b–d) the ZnO–BiOCl/TiC/PDMS samples with spin-coating the ZnO NPs solution for 3, 9, and 15 times (S3, S9, and S15).

cycles in Figure 2b, several NPs are decorated on the surface of BiOCl nanosheets. As the deposition cycles increases to 9, the SEM image of the S9 sample in Figure 2c depicts a much denser decoration of NPs. For the S15 sample in Figure 2d, the overaccumulated NPs begin to aggregate on the surface of BiOCl nanosheet, which cause the formation of several nanoislands. Some of the cavities framed by the surrounding BiOCl nanosheets may also be filled up by these NPs. The SEM images of S6 and S12 samples are shown in Figure S2b,c (Supporting Information), it is clearly revealed that the concentration of NPs grew denser on the BiOCl nanosheets with the increase of deposition cycles.

Figure 3a–c displays the transmission electron microscopy (TEM) images of the nanosheet separated from the S9 sample. It is seen that several NPs with diameters of ≈ 10 nm were evenly distributed on the surface and edge of the BiOCl nanosheet. High-resolution TEM (HRTEM) image in Figure 3d demonstrates the high crystallinity of the BiOCl nanosheet. One set of clear lattice fringes with an interplanar lattice spacing of 0.275 nm correspond to the (110) atomic planes of tetragonal BiOCl. The other sets of clear lattice fringes from the NPs decorated at the edge of nanosheet with an interplanar lattice spacing of 0.260 nm correspond to the (002) atomic planes of hexagonal ZnO. The element mapping images of the nanosheet acquired from the S9 sample are depicted in Figure 3e. The color block from Bi and Cl elements with high densities confirm the component of BiOCl nanosheet. The well-dispersed color blocks with moderate density from Zn element reflect the even distribution of ZnO NPs on the nanosheet. Together with the SEM results, these TEM images prove the successful decoration of ZnO NPs on the BiOCl nanosheets.

The surface composition and the oxidation states of the BiOCl/TiC/PDMS and S9 samples are analyzed by the X-ray

photoelectron spectroscopy (XPS), the results are depicted in **Figure 4**. Figure 4a displays the survey spectrum of the BiOCl/TiC/PDMS sample and reveals the dominant existence of element Bi, O, and Cl on the sample surface. According to Figure 4b, the binding energy peaks located at 164.7 and 159.4 eV are related to the spin orbital splitting photoelectrons of Bi $4f_{5/2}$ and Bi $4f_{7/2}$, depicting the presence of Bi in the trivalent oxidation state. In Figure 4c, the binding energy peak emerging at 529.8 eV is ascribed to O 1s, revealing the presence of O^{2-} in BiOCl. Figure 4d displays the high-resolution spectra of Cl 2p, the binding energy peaks located at 198.0 and 199.6 eV can be assigned to Cl $2p_{3/2}$ and Cl $2p_{1/2}$, respectively, confirming the existence of Cl^- in BiOCl. Figure 4e reveals the survey spectrum of the S9 sample. Figure 4f displays the high-resolution spectra of Zn 2p, the binding energy peaks located at 1021.5 and 1044.6 eV can be assigned to Zn $2p_{3/2}$ and Zn $2p_{1/2}$, respectively, confirming the existence of Zn^{2+} in the S9 sample. These results further demonstrate the successful deposition of ZnO NPs on the surface of BiOCl/TiC/PDMS sample.

Figure 5a presents the scheme image of the BiOCl/PDMS PD and the BiOCl/TiC/PDMS PD, which were assembled by doctor-blading one pair of Ag pastes with a fixed distance onto the BiOCl film and the BiOCl/TiC hybrid film, respectively. The I – V characteristics of the BiOCl/PDMS PD and the BiOCl/TiC/PDMS PD in dark and under illumination with 350 nm UV light are displayed in Figure 5b. The BiOCl/PDMS PD displays a very low dark current of 6.85 fA at 5 V and a slightly increased photocurrent of 72.3 fA under 350 nm light illumination at 5 V. Under the same conditions, the addition of the $Ti_3C_2T_x$ MXene layer causes the dramatic increase of dark current and photocurrent to 8.98 and 25.4 pA, respectively. Figure 5c presents the I – t curves of the BiOCl/PDMS PD and the BiOCl/TiC/PDMS PD under intermittent 350 nm UV light illumination at 5 V bias. It is seen that the $Ti_3C_2T_x$ MXene layer functions

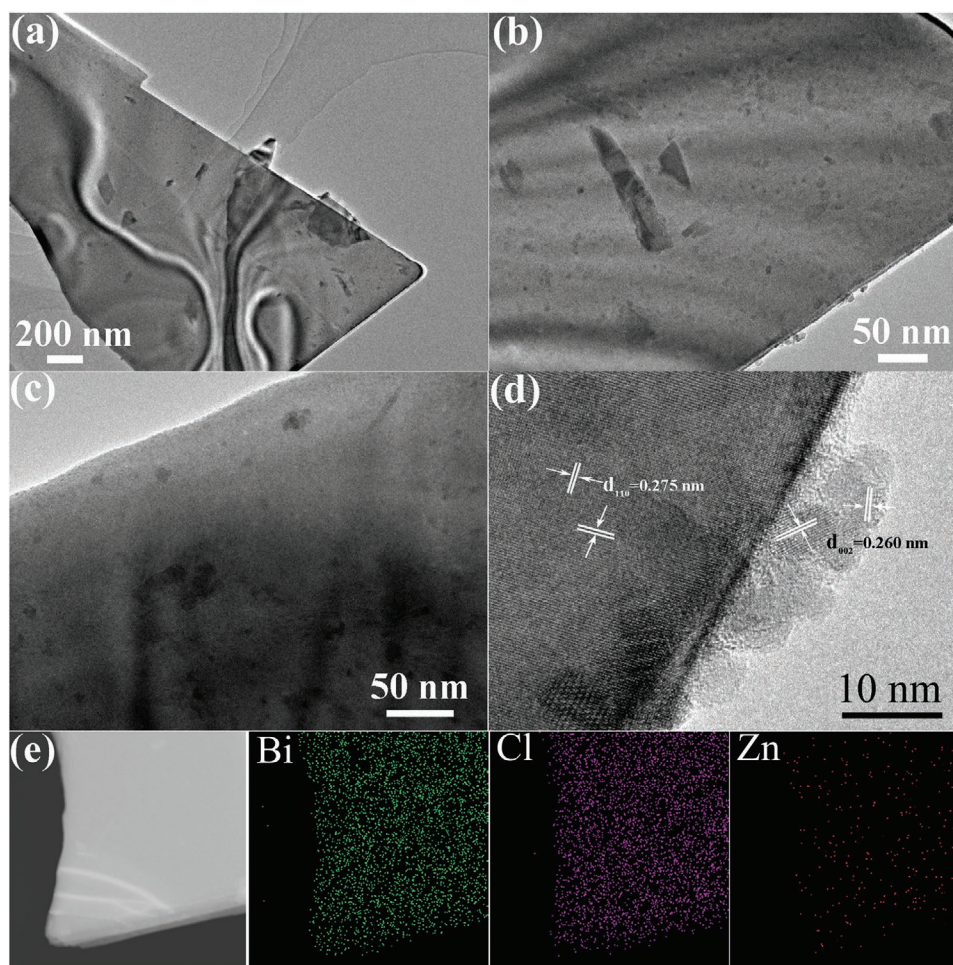


Figure 3. a–c) TEM images and d) HRTEM image of the nanosheet separated from the S9 sample. e) The element mapping images of the nanosheet acquired from the S9 sample.

as conduction additives, which increase the dark current and photocurrent by 2–3 orders of magnitude. However, the on–off ratio is decreased from 9.2 of the BiOCl/PDMS PD to 2.4 of the BiOCl/TiC/PDMS PD. As displayed in the spectral responsivities of these PDs in Figure 5d, it is shown that both PDs present UV photoresponses and their highest responsivities are achieved at 350 nm. The responsivity of BiOCl/PDMS PD at 350 nm is calculated to be $0.00917 \mu\text{A W}^{-1}$. However, the addition of $\text{Ti}_3\text{C}_2\text{T}_x$ MXene as conducting layer causes the dramatic increase of responsivities at corresponding wavelengths by 2–3 orders of magnitude. The responsivity of BiOCl/TiC/PDMS PD at 350 nm is calculated to be $2.05 \mu\text{A W}^{-1}$. It is believed that the crystal boundaries between the neighboring BiOCl nanosheets and their surface defects block the transportation charge carriers in the BiOCl/PDMS PD, which yield ultralow dark current and poor photoelectric performance. The conduction layer formed by the $\text{Ti}_3\text{C}_2\text{T}_x$ MXene flakes in the BiOCl/TiC/PDMS PD, provides novel and short conduction ways for the efficient transportation of charge carriers from the BiOCl nanosheets to the electrodes, which leads to the dramatic increase of currents. While the poor photoelectric properties of the pristine BiOCl nanosheet cause the limited generation of photoinduced electron–hole pairs upon light illumination, resulting in a small

on–off ratio. To overcome this deficiency, ZnO NPs are dispersed on the BiOCl nanosheets to build heterostructures, so as to improve the photoelectric performance of BiOCl-based PDs.

Figure 6a displays the electrode configuration of the ZnO–BiOCl/TiC/PDMS PD. The influences of different deposition amount of ZnO NPs on the photoelectric performance of these PDs were examined. Figure 6b presents the I – V characteristics of these PDs under dark and 350 nm light illumination. The S3 PD with three deposition cycles yields a much lower dark current of 0.109 pA at 5 V, which is reduced by three orders of magnitude compared with that of the BiOCl/TiC/PDMS PD. While its photocurrent at 5 V bias is increased to 65.8 pA, which is ≈ 2 –3 times high than that of the BiOCl/TiC/PDMS PD. With the increase of deposition cycles, the photocurrents at 5 V bias of the S6 and S9 PDs increase successively from 290 to 731 pA, while the dark currents remain to be ≈ 0.1 pA at 5 V. The dark currents of the S12 and S15 PDs are close to that of the S9 PD, while the further increase of deposition cycles in the S12 and S15 PDs lead to the decrease of photocurrents from 504 to 151 pA. Figure 6c shows the time-dependent current curves of different PDs with on/off switching upon 350 nm light illumination under a bias of 5 V. For all the PDs, when the light is turned on, the currents immediately increase and then reach

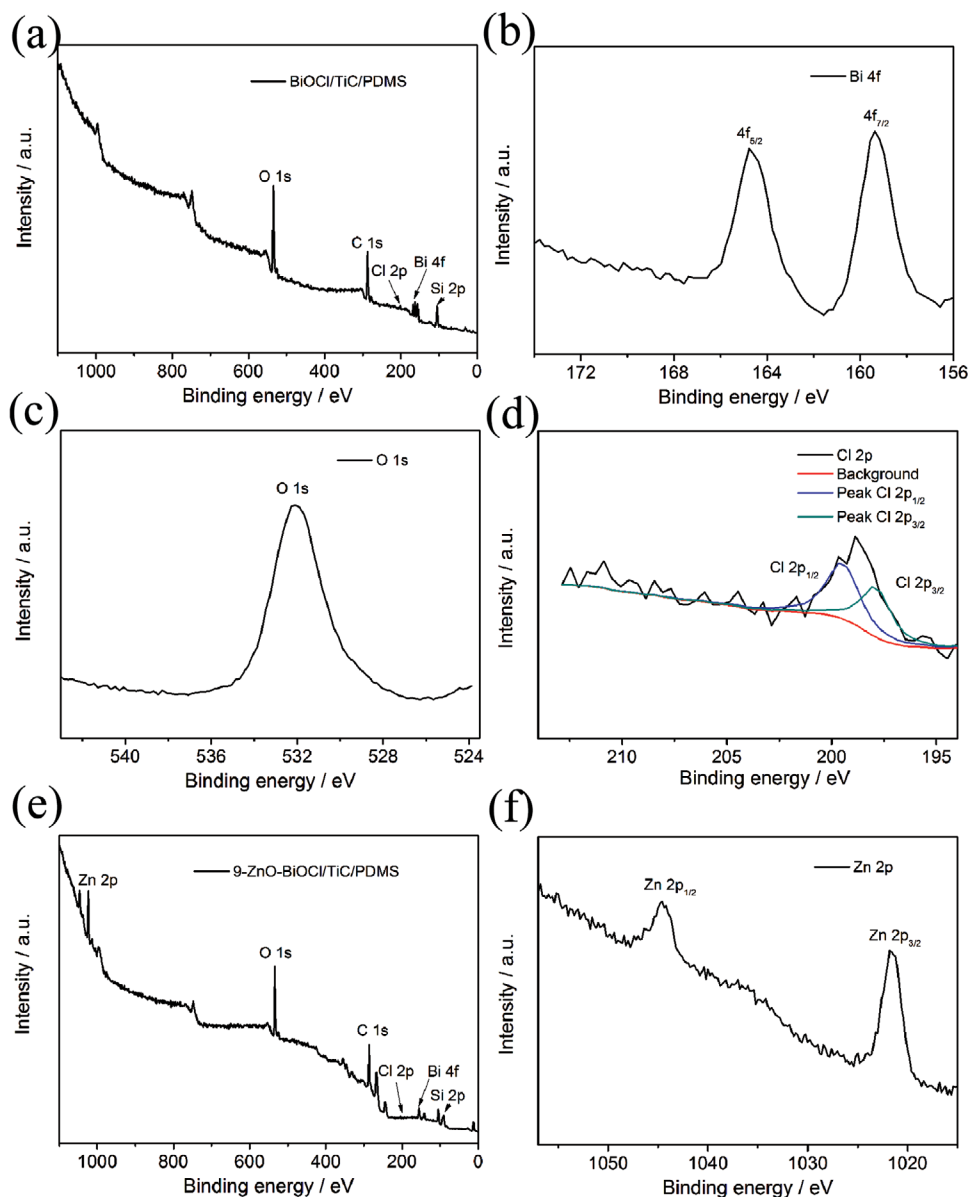


Figure 4. XPS spectra of the BiOCl/TiC/PDMS sample: a) survey scan, b) Bi 4f, c) O 1s, and d) Cl 2p spectrum. XPS spectra of the S9 sample: e) survey scan and f) Zn 2p spectrum.

steady states. The current of S3 PD at 5 V bias increases immediately from 0.095 to 49.5 pA upon the 350 nm UV light illumination. Due to the dramatic decrease of dark current caused by the deposition of ZnO NPs on the BiOCl nanosheet arrays, the on/off ratio of this PD reaches 521.1, which is much higher than those of the BiOCl/TiC/PDMS PD and the BiOCl/PDMS PD. With the increase of deposition cycles in the S6 and S9 PDs, the on/off ratio increases successively from 1519.8 to 7996.5. However, the overloaded ZnO NPs in the S12 and S15 PDs cause the decrease of the photocurrent from 484 to 144 pA and the reduction of the on/off ratio from 4322.2 to 2503.4. The currents of these heterojunction PDs can be reproduced when the light source is switched on/off repeatedly, which demonstrates the moderate stabilities of these PDs. Fast responses to light illumination are basic requirements for high performance PDs.

To investigate the influence of loading amount of ZnO NPs on the response time, the $I-t$ curves of these PDs were normalized and displayed in Figure 6d. It is calculated that the rise and decay times of the BiOCl/PDMS PD are 1.39 and 2.30 s, respectively. The addition of $\text{Ti}_3\text{C}_2\text{T}_x$ MXene conduction layer causes the decrease of rise time to 1.06 s and the increase of decay time to 6.87 s in the BiOCl/TiC/PDMS PD. In comparison, the S3 PD displays a prolonged rise time of 4.51 s and a shorted decay time of 4.68 s. The increased deposition amount of ZnO NPs causes the successive decrease of rise times from 3.12 to 2.59 s in the S6 and S9 PDs, while their decay times decrease from 2.81 to 0.93 s. Then the S12 PD displays an increased rise time of 4.23 s, and a prolonged decay time of 1.40 s. For the S15 PD, the rise and decay times are calculated to be 2.75 and 3.53 s, respectively. It is demonstrated that the optimized deposition

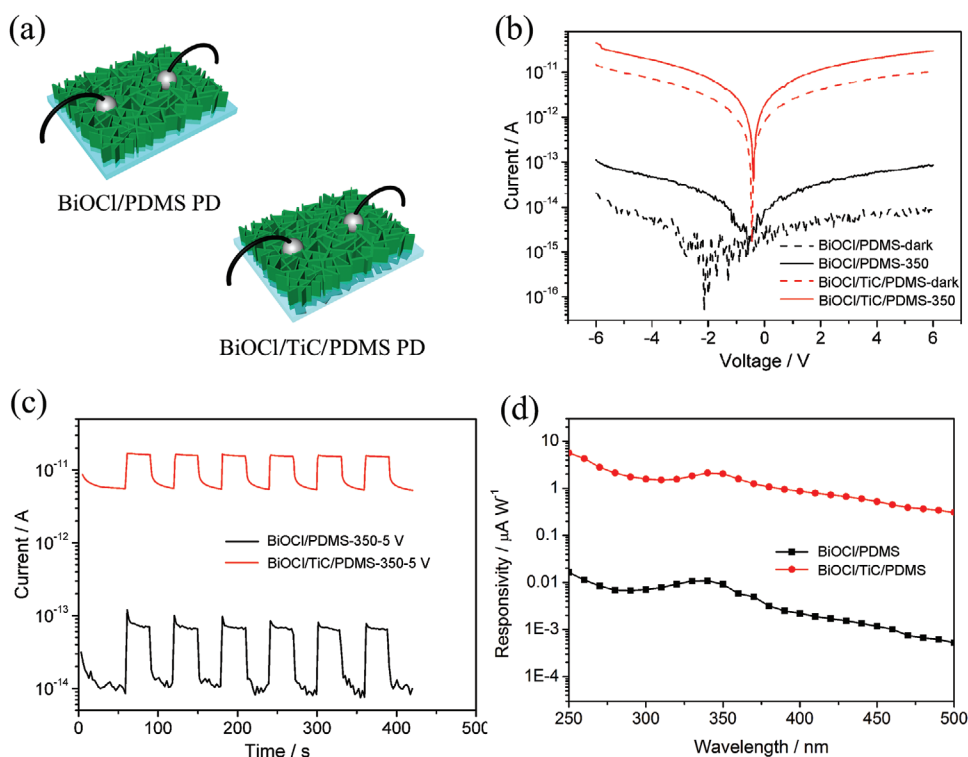


Figure 5. a) Schematic diagrams of the BiOCl/PDMS PD and the BiOCl/TiC/PDMS PD. b) I - V characteristics of the PDs in dark and under 350 nm UV light illumination. c) I - t characteristics of the PDs at 5 V bias under 350 nm intermittent UV light illumination. d) Spectral response of the PDs at 5 V bias.

of ZnO NPs can promote the rapid decay of photocurrent in the BiOCl-based PDs.

The spectral responsivity (R_λ) can be utilized to evaluate the photodetecting performance of the PDs, presenting how efficiently a detector responds to optical signals. It can be calculated by the following equation

$$R_\lambda = \frac{I_{\text{ph}} - I_{\text{d}}}{PS} \quad (1)$$

where I_{ph} is the photocurrent, I_{d} is the dark current, P is the light power density, and S is the effective irradiation area. Figure 6e presents the spectral response of these PDs at 5 V bias from 250 to 500 nm. All the PDs show distinct photore-sponse from 250 to 400 nm while display pretty low responsivities to light above 400 nm, indicating their significant UV light selectivity. With the successive increase of deposition cycles from 3 to 6 and 9, the responsivities at corresponding wavelengths ranging from 250 to 400 nm increase dramatically and the highest responsivities are achieved at 340 nm. The responsivity of the S9 PD at 340 nm reaches to $94.2 \mu\text{A W}^{-1}$, which is 46-fold higher than that of the BiOCl/TiC/PDMS PD. The continuous loading of ZnO NPs decrease the responsivities of S12 and S15 PD at 340 nm to 81.2 and $22.6 \mu\text{A W}^{-1}$, respectively. It is deduced from Figure S3a (Supporting Information) that the excess loading of ZnO NPs on the surface of BiOCl nanosheet arrays in S12 and S15 PDs inevitably reduces their light absorption, causing the decrease of responsivities.

The detectivity (D^* , typically quoted in Jones) represents the ability of a PD to detect weak signals from the noise environment. Considered the shot noise from the dark current is the major contributor of background noise, the detectivity can be calculated as

$$D^* = \frac{R_\lambda}{\left(\frac{2eI_{\text{d}}}{S}\right)^{1/2}} \quad (2)$$

where R_λ is the responsivity at specific wavelength, e is the elementary charge, I_{d} is the dark current, and S is the effective area under irradiation. The calculated detectivity curves of these PDs are displayed in Figure S3b (Supporting Information). Owing to the suppressed dark current and enhanced responsivity, the D^* of S9 PD achieves as high as 5.86×10^{10} Jones at 350 nm, which is the highest value of D^* among all the PDs in the wavelength range of 250–400 nm, demonstrating the improved photodetecting performance caused by the optimized deposition of ZnO NPs.

The photosensitivity of the S9 PD was also examined using 350 nm UV light with power densities ranging from 0.1296 to 0.749 mW cm^{-2} . The I - V curves of the S9 PD with respect to the increased light intensities are shown in Figure 6f. The photocurrent values of the PD increase as the light intensities increase, yielding photocurrent values of 91.3 pA at $0.1296 \text{ mW cm}^{-2}$, 376.6 pA at $0.2988 \text{ mW cm}^{-2}$, 562.6 pA at 0.527 mW cm^{-2} , 598.1 pA at 0.67 mW cm^{-2} , and 640.0 pA at 0.749 mW cm^{-2} for 350 nm UV light at 5 V. This result matches

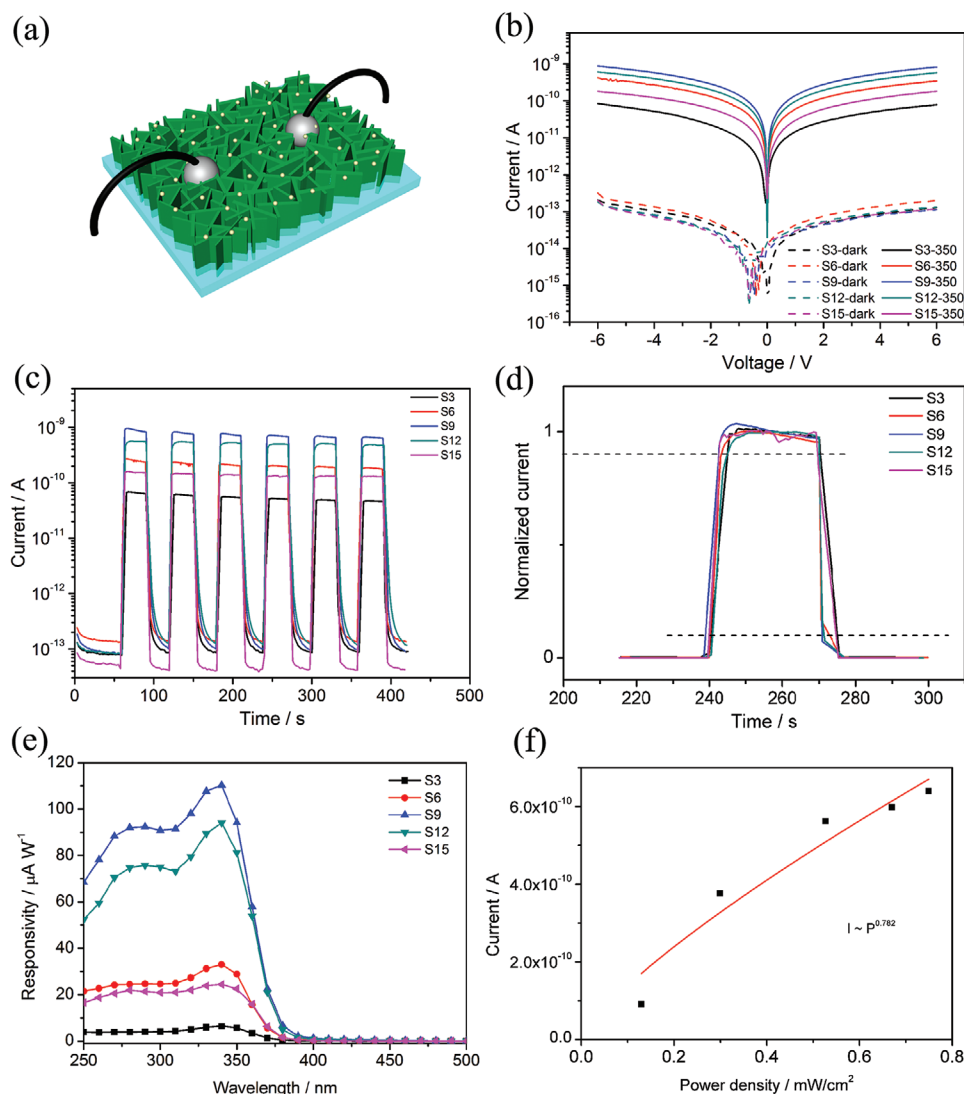


Figure 6. a) Schematic diagram of the ZnO–BiOCl/TiC/PDMS PDs (S3–S15). b) I – V characteristics of these PDs under dark and 350 nm light illumination. c) I – t characteristics of these PDs at 5 V bias under 350 nm intermittent light illumination. d) The normalized I – t curve of these PDs at 5 V bias under 350 nm light illumination. e) Spectral response of these PDs at 5 V bias. f) Corresponding fitting curve for the relationship between the photocurrent values of the S9 PD and the light intensities of 350 nm UV light illumination

well with the proportional relationship between the photogeneration efficiency of charge carriers and the absorbed photon flux. The nonlinear relationship for the change of photocurrent against light intensity follows the power law

$$I_{\text{ph}} = AP^{\theta} \quad (3)$$

where A is a constant for a certain wavelength, and the exponent ($0.5 < \theta < 1$) determines the response of the photocurrent to light intensity. By fitting the curve in with this equation in Figure 6f, the value of θ is calculated to be 0.782 for the S9 PD at the wavelength of 350 nm and an applied voltage of 5 V.

The characteristic parameters of the BiOCl/PDMS PD, the BiOCl/TiC/PDMS PD, and different ZnO–BiOCl/TiC/PDMS PDs operated at 5 V bias under illumination of 350 nm UV light are summarized and compared in Table 1.

To investigate the function of the $\text{Ti}_3\text{C}_2\text{T}_x$ MXene layer on improving the photoelectric performance of the ZnO–BiOCl/TiC/PDMS PDs, the ZnO–BiOCl/PDMS samples are prepared without the addition of $\text{Ti}_3\text{C}_2\text{T}_x$ MXene and fabricated as the corresponding PDs. Figure S4a (Supporting Information) presents the electrode configuration of these PDs. Figure S4b,c (Supporting Information) shows the I – V and I – t characteristics of the ZnO–BiOCl/PDMS PDs under dark and 350 nm UV light illumination. The dark currents of these PDs are nearly the same with that of the BiOCl/PDMS PD. Under 350 nm light illumination, the Z6 PD achieved the highest photocurrent of 26.9 pA, which is significantly lower than that of the S9 PD. The calculated rise and decay times of the Z6 PD are 4.98 and 1.41 s, which are longer than those of the S9 PD. Figure S4d (Supporting Information) displays the spectral response of these PDs at 5 V bias from 250 to 500 nm. All the

Table 1. Comparison of the characteristic parameters of the BiOCl/PDMS PD, the BiOCl/TiC/PDMS PD, and the different ZnO–BiOCl/TiC/PDMS PDs operated at 5 V bias under 350 nm light illumination.

Sample	Photocurrent [pA]	Rise time [s]	Decay time [s]	On–off ratio	Responsivity [$\mu\text{A W}^{-1}$]	Detectivity [Jones]
BiOCl/PDMS	0.0723	1.39	2.30	9.2	0.00917	1.95×10^7
BiOCl/TiC/PDMS	25.4	1.06	6.87	2.4	2.05	1.47×10^9
S3	65.8	4.51	4.68	521.1	5.71	3.44×10^9
S6	290	3.12	2.81	1519.8	28.9	1.36×10^{10}
S9	731	2.59	0.93	7996.5	94.2	5.86×10^{10}
S12	504	4.23	1.40	4322.2	81.2	4.08×10^{10}
S15	151	2.75	3.53	2503.4	22.6	1.63×10^{10}

PDs show high UV light selective response characteristics. The Z6 PD reaches a highest responsivity of $759 \mu\text{A W}^{-1}$, which is also much lower than that of S9 PD. It is concluded that the elimination of $\text{Ti}_3\text{C}_2\text{T}_x$ MXene conduction layer can cause decreased photoresponse and prolonged response time in the ZnO–BiOCl/PDMS PDs. The $\text{Ti}_3\text{C}_2\text{T}_x$ MXene conduction layer is believed to provide a fast transport path for the carrier transport and reduce the recombination possibilities of the photoinduced charge carriers, resulting in enhanced photoresponse and fast response speed in the ZnO–BiOCl/TiC/PDMS PDs.

As illustrated in Figure S5 (Supporting Information), both the BiOCl and ZnO samples show photoabsorption in the UV zone, and the bandgaps of BiOCl and ZnO are calculated to be 3.05 and 3.31 eV, respectively. The Fermi energy bands of BiOCl and ZnO are aligned at the same position after the formation of heterojunction. It is deduced that the potential values of the conduction and valence band edge of BiOCl are more negative than those of ZnO, thus a type-II heterojunction can be formed between ZnO and BiOCl. The energy band alignment of the type-II BiOCl–ZnO heterojunction is elucidated in Figure 7a. Upon the carrier diffusion under thermal equilibrium conditions, a depletion region is developed at the interface between p-type BiOCl nanosheets and n-type ZnO NPs, the as-formed built-in electric field changes the band bending at the interface and provides a driving force for the separation of photogenerated carriers. In dark, the built-in electric field at the interface in the ZnO–BiOCl/TiC/PDMS PDs will hinder the transport of electrons between the electrodes and decrease the dark currents dramatically. Upon above-bandgap

light illumination with a wavelength range from 250 to 400 nm, the photogenerated electron–hole pairs could be separated at faster rates by the built-in electric field formed in the depletion region, as depicted in Figure 7b. Driven by this electric field, the electrons flow to the conduction band of n-type ZnO NPs, while the holes move toward the valence band of p-type BiOCl nanosheets. As demonstrated in the TEM results, a majority of ZnO NPs are deposited on the (001) facet of BiOCl nanosheets, which facilitates the direct transport of photoinduced electrons from the BiOCl phase to ZnO phase.^[52,53]

Derived from the results mentioned above, it is concluded that the increased light absorption brought by the introduction of ZnO NPs, the promoted separation caused by the formation of heterojunction between ZnO NPs and BiOCl nanosheet array, and the efficient carrier pathways provided by the $\text{Ti}_3\text{C}_2\text{T}_x$ MXene conduction layers, contribute to the greatly improved photoresponse and response speed of the ZnO–BiOCl/TiC/PDMS PDs. Considered the flexibility of PDMS substrate, the photoresponses of S9 PDs at different bend-states are tested and the results are shown in Figure S6 (Supporting Information). As the bending angle turns from 180° (original state) to 120° , the photocurrent under 350 nm light illumination at 5 V bias decreases dramatically from 739 to 3 pA. The dramatic decrease of photocurrent can be ascribed to the structural damage of BiOCl nanosheet array along with the deformation of PDMS substrate at the bend states. The further bending of the PDMS substrate to 90° and 60° , develops cracks on the surface of PDMS substrate and breaks the linkage of the BiOCl nanosheet array embedded into the substrate, decreasing the

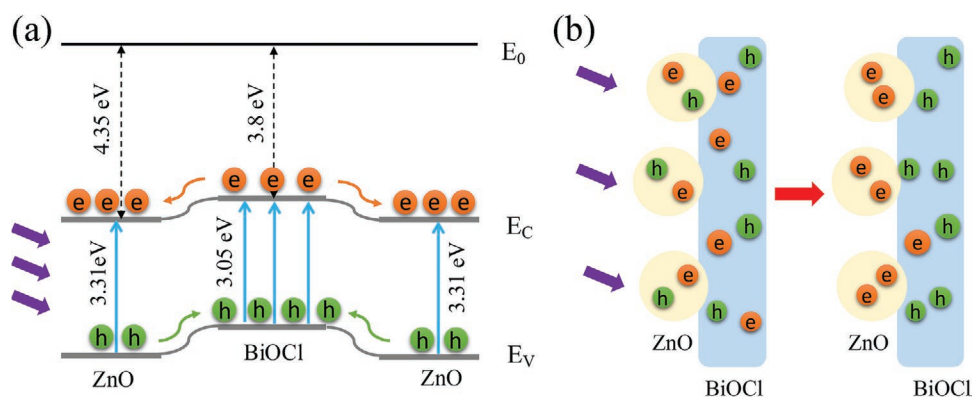


Figure 7. a) Energy band alignments and b) schematics of carrier separation mechanism in the ZnO–BiOCl/TiC/PDMS PD upon UV illumination.

photocurrents continuously to 0.7 and 0.6 pA. After the PDMS substrate is released from the bend state, the BiOCl nanosheets near the cracks come back into contact and the conducting pathway for carrier is partly rebuilt, thus the photocurrent of S9 PD increases to 1 pA. Further effects should be spared to improve the integrity of BiOCl nanostructures on flexible substrate and impose the BiOCl-based PDs with good mechanical properties.

3. Conclusions

Large-area BiOCl nanosheet arrays grown on Cu substrate were transferred onto the PDMS substrate by the simple etching of Cu foil and curing of the PDMS. The as-fabricated BiOCl/PDMS PD shows very poor photoelectric performance with a photocurrent of 670 fA under 350 nm light illumination at 5 V. The addition of a $\text{Ti}_3\text{C}_2\text{T}_x$ MXene conduction layer improves both the values of photocurrent and dark current by 2–3 orders of magnitude. While this BiOCl/TiC/PDMS PD suffers from a large dark current (6.7 pA), a low on–off ratio (2.40), and long decay time (6.87 s) under the same conditions. After it is decorated with optimized amount of ZnO NPs, the S9 PD achieves a low dark current of 86 fA, a high on–off ratio of 7996.5, and a short decay time of 0.93 s. While the elimination of the $\text{Ti}_3\text{C}_2\text{T}_x$ MXene layer causes the decreased photocurrents and prolonged decay times of the ZnO–BiOCl/PDMS PDs. It is concluded that the greatly improved photoresponse and response speed of the ZnO–BiOCl/TiC/PDMS PDs are ascribed to the increased light absorption brought by the deposition of ZnO NPs, the promoted carrier separation caused by the heterojunction formed between ZnO NPs and BiOCl nanosheet array, and the efficient carrier pathways provided by the $\text{Ti}_3\text{C}_2\text{T}_x$ MXene conduction layers. It is demonstrated that the construction of heterojunctions with metal oxide semiconductors and the introduction of conduction additives improve the photodetecting performance of BiOCl-based PDs, paving ways for their practical applications in the photoelectric devices.

4. Experimental Section

All the chemical reagents were bought from the Sinopharm Company and Dow Chemical Company, these chemical reagents were used without further purification.

Preparation of BiOCl Film on Cu Foil: A piece of copper foil with a surface area of $4 \times 2 \text{ cm}^2$ was cleaned in absolute alcohol and then dried at 60 °C. 0.315 g of BiCl_3 and 3.3 mL of concentrated HCl were added into a mixture solution of 10 mL of ethylene glycol and 84 mL of H_2O . The mixed solution was heated by water bath to 70 °C while stirring. Then, 2 mL of 30% H_2O_2 solution was added drop-wisely into this mixture solution. Several minutes later, the copper foil was immersed in this solution and kept for 1 h. After the foil was taken out, washed by absolute alcohol for several times, and dried at 60 °C for several hours, the BiOCl/Cu sample was obtained.

Preparation of BiOCl Film on PDMS Substrate: The BiOCl film on one side of the BiOCl/Cu sample was removed by sharp blade. Certain amount of PDMS precursor was prepared by mixing Sylgard 184 silicone elastomer and the corresponding curing agent from Dow Corning Corporation with a fixed mass ratio of 10:1. This PDMS precursor was degassed and dipped on the BiOCl/Cu sample. After the PDMS precursor was spread out evenly, the hybrid was degassed again

and then cured at 90 °C for 3 h. To remove the Cu foil, the hybrid was immersed into 30 mL of 0.1 g mL^{-1} FeCl_3 aqueous solution for 12 h. After the reaction and dissolution of Cu foil, the hybrid was taken out, washed with H_2O and alcohol for several times, and dried at 60 °C. Then the BiOCl/PDMS sample with a film thickness of ca. 0.5–0.8 mm was obtained.

Preparation of the BiOCl/TiC/PDMS Sample: 2 g of LiF was added to 40 mL of 9 M HCl solution and stirred for half an hour. After the addition of 2 g of Ti_3AlC_2 powder the mixture was heated to 35 °C and stirred for 24 h. Then, the mixture was then centrifuged at 3500 rpm for 10 min. After the removal of supernatant, the precipitate was sonicated in de-ioned water with a power of 750 W for 10 min and then washed with de-ioned water for several times. After the addition of absolute alcohol into the above precipitation, the mixture was sonicated for 1 h and was then centrifuged at 10000 rpm for 10 min. With the addition of certain amount of de-ioned water, the mixture was sonicated at a power of 750 W for 20 min. Then, the supernatant was collected, washed, and centrifuged at 3500 rpm for several times, until a stable colloid solution of $\text{Ti}_3\text{C}_2\text{T}_x$ MXene was formed. The concentration of $\text{Ti}_3\text{C}_2\text{T}_x$ MXene in this solution is estimated to be 0.355 g mL^{-1} . After the BiOCl film on one side of BiOCl/Cu sample was removed by sharp blade, a certain amount of $\text{Ti}_3\text{C}_2\text{T}_x$ MXene aqueous solution was deposited on the BiOCl/Cu sample by spin-coating at 2000 rpm for 20 s and three times before drying at 60 °C for several hours. The stocking PDMS precursor mixture was degassed and dipped onto the above TiC/BiOCl/Cu sample. After the PDMS precursor was spread out evenly, the hybrid was degassed and then heated at 90 °C for 3 h for curing. After being immersed into 30 mL of 0.1 g mL^{-1} FeCl_3 aqueous solution to remove the Cu foil, the hybrid was taken out of the solution, washed with de-ioned water and absolute alcohol for several times, and dried at 60 °C. Then the BiOCl/TiC/PDMS sample was obtained.

Preparation of the ZnO–BiOCl/TiC/PDMS and ZnO–BiOCl/PDMS Samples: ZnO NPs were prepared by a modified hydrolysis method in methanol. 2.95 g of $\text{Zn}(\text{CH}_3\text{COO})_2 \cdot 2\text{H}_2\text{O}$ was dissolved in 125 mL of methanol at 60 °C. 1.57 g of KOH was dispersed in 65 mL of methanol to form a KOH solution and it was added to the above solution within 5 min. After stirring for around 1.5 h, the reaction solution turned from transparent to turbid, the reaction mixture was then stirred for another hour. The as-obtained NPs were collected by centrifugation and washed by methanol for three times. The precipitate was then dispersed in methanol to form the ZnO NPs solution with an estimated concentration of 18 mg mL^{-1} . The above solution was spin-coated on the BiOCl/TiC/PDMS sample for different cycles to acquire a series of ZnO–BiOCl/TiC/PDMS samples. The sample with 3, 6, 9, 12, and 15 deposition cycles are denoted as S3, S6, S9, S12, and S15. For comparison, the ZnO NPs were also deposited on the BiOCl/PDMS sample for 3, 6, and 9 cycles, the corresponding ZnO–BiOCl/PDMS samples are denoted as Z3, Z6, and Z9.

Analysis Instruments: X-ray diffraction (XRD) patterns of the samples were collected on a Bruker D8-A25 diffractometer using Cu $K\alpha$ radiation ($\lambda = 1.5405 \text{ \AA}$) to probe their crystal structures. A field-emission scanning electron microscopy (FESEM, Zeiss Sigma) and a high-resolution transmission electron microscopy (HRTEM, TECNAI G2 S-TWIN) were used to examine the morphology and microstructures of the samples, respectively. X-ray photoelectron spectroscopy (E Perkin Elmer PHI 5000 C ESCA system equipped with a hemispherical electron energy analyzer) was utilized to investigate the composition and chemical state of the samples. The binding energy for C 1s peak at 284.6 eV was used as the reference for calibration. A Hitachi U3900H spectrophotometer using Al_2O_3 as a reference was used to conduct the UV–vis spectroscopy.

Photoelectric Measurements: Two pieces of silver pastes with fixed area and distance were doctor-bladed onto the composites films as two electrodes of PDs. The current–voltage characteristic and the current-time transient response were conducted on a program-controlled semiconductor characterization system (Keithley 4200SCS, USA) to characterize the photoelectric properties of the as-constructed PDs. A 75 W Xe lamp equipped with a monochromator was utilized as the light source, and a NOVA II power meter (OPHIR photonics) was

used to measure the light power density. All these measurements were conducted under ambient conditions.

Bending Test: Several rectangular Cu foils with the same sizes were bended to different states (bending angles of 180°, 120°, 90°, and 60°) from the symmetry axis. Then, as depicted in Figure S6 (Supporting Information), the S9 PD was fixed onto the first bended Cu foil (bending angle of 180°) conformally by double sided adhesive tape, while keeping the symmetry axis of Cu foils in coincident with that of the two silver paste electrodes in S9 PD. After the photoelectric test at this bent state, the S9 PD was moved up and fixed onto the other bended Cu foils in sequences, corresponding photoelectric tests at these bent states and the recovery state were conducted in turns.

Supporting Information

Supporting Information is available from the Wiley Online Library or from the author.

Acknowledgements

The authors acknowledge the support from the National Key R&D Program of China (Grant Nos. 2017YFA0204600 and 2018YFA0703700), the National Natural Science Foundation of China (Grant Nos. 51872050 and 11674061), the China Postdoctoral Science Foundation (Grant Nos. 2018M640338 and 2019T120299), and Science and Technology Commission of Shanghai Municipality (Grant Nos. 19520744300, 18520744600, and 18520710800). Part of the experimental work was carried out in the Fudan Nanofabrication Laboratory.

Conflict of Interest

The authors declare no conflict of interest.

Keywords

BiOCl nanosheet arrays, heterojunctions, $\text{Ti}_3\text{C}_2\text{T}_x$ MXene, UV photodetectors, ZnO nanoparticles

Received: February 15, 2020

Revised: April 4, 2020

Published online: May 18, 2020

- [1] J. Li, Y. Yu, L. Z. Zhang, *Nanoscale* **2014**, *6*, 8473.
- [2] Z. W. Wang, M. Chen, D. L. Huang, G. M. Zeng, P. Xu, C. Y. Zhou, C. Lai, H. Wang, M. Cheng, W. J. Wang, *Chem. Eng. J.* **2019**, *374*, 1025.
- [3] F. P. García de Arquer, O. S. Bushuyev, P. De Luna, C.-T. Dinh, A. Seifitokaldani, M. I. Saidaminov, C.-S. Tan, L. N. Quan, A. Proppe, M. G. Kibria, S. O. Kelley, D. Sinton, E. H. Sargent, *Adv. Mater.* **2018**, *30*, 1802858.
- [4] W. Li, Y. Xu, Y. L. Dong, Y. H. Wu, C. L. Zhang, M. Zhou, Q. Fu, M. H. Wu, Y. Lei, *Chem. Commun.* **2019**, *55*, 6507.
- [5] J. Li, H. Li, G. M. Zhan, L. Z. Zhang, *Acc. Chem. Res.* **2017**, *50*, 112.
- [6] S. S. M. Bhat, H. W. Jang, *ChemSusChem* **2017**, *10*, 3001.
- [7] J. Di, J. X. Xia, H. M. Li, S. J. Guo, S. Dai, *Nano Energy* **2017**, *41*, 172.
- [8] L. S. Gómez-Velázquez, A. Hernández-Gordillo, M. J. Robinson, V. J. Leppert, S. E. Rodil, M. Bizarro, *Dalton Trans.* **2018**, *47*, 12459.
- [9] L. J. Zhao, X. C. Zhang, C. M. Fan, Z. H. Liang, P. D. Han, *Phys. B* **2012**, *407*, 3364.
- [10] D. S. Bhachu, S. J. A. Moniz, S. Sathasivam, D. O. Scanlon, A. Walsh, S. M. Bawaked, M. Mokhtar, A. Y. Obaid, I. P. Parkin, J. W. Tang, C. J. Carmalt, *Chem. Sci.* **2016**, *7*, 4832.
- [11] Z. Z. Lou, P. Wang, B. B. Huang, Y. Dai, X. Y. Qin, X. Y. Zhang, Z. Y. Wang, Y. Y. Liu, *ChemPhotoChem* **2017**, *1*, 136.
- [12] J. Jiang, K. Zhao, X. Y. Xiao, L. Z. Zhang, *J. Am. Chem. Soc.* **2012**, *134*, 4473.
- [13] C. F. Guo, J. M. Zhang, Y. Tian, Q. Liu, *ACS Nano* **2012**, *6*, 8746.
- [14] J. Li, Y. R. Li, *ChemistrySelect* **2018**, *3*, 4512.
- [15] Y. Y. Li, J. P. Liu, J. Jiang, J. G. Yu, *Dalton Trans.* **2011**, *40*, 6632.
- [16] F. Teng, W. X. Ouyang, Y. M. Li, L. X. Zheng, X. S. Fang, *Small* **2017**, *13*, 1700156.
- [17] W. X. Ouyang, F. Teng, X. S. Fang, *Adv. Funct. Mater.* **2018**, *28*, 1707178.
- [18] M. Li, J. Y. Zhang, H. Gao, F. Li, S.-E. Lindquist, N. Q. Wu, R. M. Wang, *ACS Appl. Mater. Interfaces* **2016**, *8*, 6662.
- [19] C. H. Gong, K. Hu, X. P. Wang, P. H. Wangyang, C. Y. Yan, J. W. Chu, M. Liao, L. P. Dai, T. Y. Zhai, C. Wang, L. Li, J. Xiong, *Adv. Funct. Mater.* **2018**, *28*, 1706559.
- [20] S. Y. Li, Y. Zhang, W. Yang, H. Liu, X. S. Fang, *Adv. Mater.* **2020**, *32*, 1905443.
- [21] W. X. Ouyang, L. X. Su, X. S. Fang, *Small* **2018**, *14*, 1801611.
- [22] B. W. Zhu, Z. Q. Niu, H. Wang, W. R. Leow, H. Wang, Y. G. Li, L. Y. Zheng, J. Wei, F. W. Huo, X. D. Chen, *Small* **2014**, *10*, 3625.
- [23] Q. Wang, M. Q. Jian, C. Y. Wang, Y. Y. Zhang, *Adv. Funct. Mater.* **2017**, *27*, 1605657.
- [24] M. Alhabeab, K. Maleski, B. Anasori, P. Lelyukh, L. Clark, S. Sin, Y. Gogotsi, *Chem. Mater.* **2017**, *29*, 7633.
- [25] J. Zhou, X. H. Zha, M. Yildizhan, P. Eklund, J. M. Xue, M. Y. Liao, P. O. Å. Persson, S. Y. Du, Q. Huang, *ACS Nano* **2019**, *13*, 1195.
- [26] H. Wang, Y. Wu, X. Z. Yuan, G. M. Zeng, J. Zhou, X. Wang, J. W. Chew, *Adv. Mater.* **2018**, *30*, 1704561.
- [27] X. B. Yan, K. Y. Wang, J. H. Zhao, Z. Y. Zhou, H. Wang, J. J. Wang, L. Zhang, X. Y. Li, Z. A. Xiao, Q. L. Zhao, Y. F. Pei, G. Wang, C. Y. Qin, H. Li, J. Z. Lou, Q. Liu, P. Zhou, *Small* **2019**, *15*, 1900107.
- [28] Y. C. Cai, J. Shen, G. Ge, Y. Z. Zhang, W. Q. Jin, W. Huang, J. J. Shao, J. Yang, X. C. Dong, *ACS Nano* **2018**, *12*, 56.
- [29] S. J. Kim, H.-J. Koh, C. E. Ren, O. Kwon, K. Maleski, S.-Y. Cho, B. Anasori, C.-K. Kim, Y.-K. Choi, J. Kim, Y. Gogotsi, H.-T. Jung, *ACS Nano* **2018**, *12*, 986.
- [30] D. B. Velusamy, J. K. El-Demellawi, A. M. El-Zohry, A. Giugni, S. Lopatin, M. N. Hedhili, A. E. Mansour, E. D. Fabrizio, O. F. Mohammed, H. N. Alshareef, *Adv. Mater.* **2019**, *31*, 1807658.
- [31] Y. Dong, S. S. K. Mallineni, K. Maleski, H. Behlow, V. N. Mochalin, A. M. Rao, Y. Gogotsi, R. Podila, *Nano Energy* **2018**, *44*, 103.
- [32] H. C. Fu, V. Ramalingam, H. Kim, C. H. Lin, X. S. Fang, H. N. Alshareef, J. H. He, *Adv. Energy Mater.* **2019**, *9*, 1900180.
- [33] J. Yang, W. Z. Bao, P. Jaumaux, S. T. Zhang, C. Y. Wang, G. X. Wang, *Adv. Mater. Interfaces* **2019**, *6*, 1802004.
- [34] M.-Q. Zhao, M. Torelli, C. E. Ren, M. Ghidui, Z. Ling, B. Anasori, M. W. Barsoum, Y. Gogotsi, *Nano Energy* **2016**, *30*, 603.
- [35] H. H. Tang, H. R. Feng, H. K. Wang, X. J. Wan, J. J. Liang, Y. S. Chen, *ACS Appl. Mater. Interfaces* **2019**, *11*, 25330.
- [36] S. Chertopalov, V. N. Mochalin, *ACS Nano* **2018**, *12*, 6109.
- [37] Z. Kang, Y. N. Ma, X. Y. Tan, M. Zhu, Z. Zheng, N. S. Liu, L. Y. Li, Z. G. Zou, X. L. Jiang, T. Y. Zhai, Y. H. Gao, *Adv. Electron. Mater.* **2017**, *3*, 1700165.
- [38] W. Deng, H. C. Huang, H. M. Jin, W. Li, X. Chu, D. Xiong, W. Yan, F. J. Chun, M. L. Xie, C. Luo, L. Jin, C. Q. Liu, H. T. Zhang, W. L. Deng, W. Q. Yang, *Adv. Opt. Mater.* **2019**, *7*, 1801521.
- [39] Y. J. Yang, J. Jeon, J.-H. Park, M. S. Jeong, B. H. Lee, E. Hwang, S. Lee, *ACS Nano* **2019**, *13*, 8804.
- [40] Z. H. Long, X. J. Xu, W. Yang, M. X. Hu, D. V. Shtansky, D. Golberg, X. S. Fang, *Adv. Electron. Mater.* **2020**, *6*, 1901048.

- [41] J. X. Chen, W. Ouyang, W. Yang, J. H. He, X. S. Fang, *Adv. Funct. Mater.* **2020**, *30*, 1909909.
- [42] W. Yang, K. Hu, F. Teng, J. H. Weng, Y. Zhang, X. S. Fang, *Nano Lett.* **2018**, *18*, 4697.
- [43] Y.-X. Yu, W.-X. Ouyang, W.-D. Zhang, *J. Solid State Electrochem.* **2014**, *18*, 1743.
- [44] Y.-X. Yu, W.-X. Ouyang, Z.-T. Liao, B.-B. Du, W.-D. Zhang, *ACS Appl. Mater. Interfaces* **2014**, *6*, 8467.
- [45] W. X. Ouyang, F. Teng, J.-H. He, X. S. Fang, *Adv. Funct. Mater.* **2019**, *29*, 1807672.
- [46] C. Sa, X. Xu, X. Wu, J. Chen, C. Zuo, X. S. Fang, *J. Mater. Chem. C* **2019**, *7*, 13097.
- [47] F. Teng, L. X. Zheng, K. Hu, H. Y. Chen, Y. M. Li, Z. M. Zhang, X. S. Fang, *J. Mater. Chem. C* **2016**, *4*, 8416.
- [48] B. Zhao, F. Wang, H. Y. Chen, L. X. Zheng, L. X. Su, D. X. Zhao, X. S. Fang, *Adv. Funct. Mater.* **2017**, *27*, 1700264.
- [49] Z. W. Jin, Q. Zhou, Y. H. Chen, P. Mao, H. Li, H. B. Liu, J. Z. Wang, Y. L. Li, *Adv. Mater.* **2016**, *28*, 3697.
- [50] K. Hu, F. Teng, L. X. Zheng, P. P. Yu, Z. M. Zhang, H. Y. Chen, X. S. Fang, *Laser Photonics Rev.* **2017**, *11*, 1600257.
- [51] K. Shen, X. Li, H. Xu, M. Q. Wang, X. Dai, J. Guo, T. Zhang, S. B. Li, G. F. Zou, K.-L. Choy, I. P. Parkin, Z. X. Guo, H. Y. Liu, J. Wu, *J. Mater. Chem. A* **2019**, *7*, 6134.
- [52] T. Li, X. C. Zhang, C. M. Zhang, R. Li, J. X. Liu, R. Lv, H. Zhang, P. D. Han, C. M. Fan, Z. F. Zheng, *Phys. Chem. Chem. Phys.* **2019**, *21*, 868.
- [53] S. Bai, L. L. Wang, Z. Q. Li, Y. J. Xiong, *Adv. Sci.* **2017**, *4*, 1600216.